Efficiency Characteristic and Operating Area of High-Power Reconfigurable Batteries

Jan Engelhardt, *Member, IEEE,* Jan Martin Zepter, *Member, IEEE,*, Mattia Marinelli, *Senior Member, IEEE,*, Luigi Piegari, *Senior Member, IEEE,*

***Abstract*—Reconfigurable batteries can change their cell topology in real time, which enables them to adapt their voltage during operation. This unique capability makes interfacing power converters redundant in applications where batteries are directly coupled with other DC components or systems. The present paper characterizes a 104 kWh prototype of a reconfigurable battery for high power applications, and derives equations for calculating the battery efficiency for the complete operating area. The battery can adapt its voltage from 0 V up to 1200 V, and reaches power values of 240 kW for charging, and 280 kW for discharging. The results are presented in efficiency maps, showing the dependency on voltage, power, and state of charge. Moreover, the efficiency characteristic is compared to a conventional battery with fixed cell topology and DC-DC converter. The reconfigurable battery can operate at a wider voltage range and achieves better efficiency up to an average power of 44.6 kW during charging, and 46.7 kW during discharging. Conversely, the conventional system performs better above these thresholds. Finally, the presented model can be used to optimize the design of reconfigurable battery strings, and to accurately size such systems for specific applications and purposes.**

***Index Terms*—battery characterization, battery losses, cell balancing, dc-dc converter, energy storage, Thevenin equivalent.**

I. Introduction

Battery storage systems are considered key elements of future electricity grids. With an increasing share of variable and partly uncontrollable renewable energy generation, their balancing capability helps to ensure stable and reliable grid operation [1], [2]. Batteries can further be utilized as power buffers for grid components with high peak load demand, such as electric vehicle (EV) fast charging stations [3]. Therefore, there has been increasing interest in combining fast-charging stations with battery systems and renewable energy sources [4], [5]. The battery storage enables the local usage of renewable energy and at the same time mitigates the impact of high power charging on the grid [6]. The different components are usually connected to a common bus using individual power converters, which are necessary to convert the voltage level and to actively control the power flow [7], [8].

In the past years, the concept of reconfiguable batteries has emerged as an alternative design solution for conventional battery energy storage systems (BESS). The cells of reconfigurable batteries are equipped with semiconductor switches, which allow to dynamically modify the topology of the battery during operation. While this increases the design complexity, it tackles typical challenges exhibited by conventional BESS, in particular cell unbalance issues, and the fact that the system performance is often constrained by single cells [9]. The variable topology further provides the battery with the intrinsic capability of adjusting its voltage. This could make power converters redundant in applications where batteries are directly coupled with other DC components or systems, saving investment costs and possibly power losses.

While the concept of reconfigurable batteries has been discussed in [10] and [11], real-life implementations are essential for assessing their feasibility. Ji et al. [12] conducted an experimental study with a small-scale reconfigurable battery comprising 9 cells (2.2 Ah each), directly coupled to a DC load. The results showed that the battery could achieve good cell equalization while maintaining low voltage fluctuations without any DC-DC converters. However, the application in grid-integrated battery systems requires implementations of larger scale. To this end, the present work investigates a 104 kWh prototype of a reconfigurable battery string, developed within the research projects INSULAE and TOPChargE. In 2021, a BESS comprising three of those strings has been installed for field tests on the Danish island of Bornholm [13]. The strings can be individually connected to other DC components through a busbar matrix: a photovoltaic (PV) system, two EV fast chargers, and a grid-tie inverter. The general working principle of the reconfigurable string design has been previously shown through simulations [14], and the prototype on the demonstration site has charged hundreds of EVs since installation [15].

To seamlessly integrate this battery technology as controllable power units in a wide range of system applications, comprehensive knowledge on the operating area and the efficiency is essential. To this end, Engelhardt et al. [16] introduced general equations for deriving the efficiency characteristic of reconfigurable batteries. The present work is an extended version of this conference paper, and provides additional key insights on string design and efficiency characteristic. In particular, the string topology proposed in the present paper considers an additional degree of freedom. The design comprises two substrings, which can be either connected in series or parallel to adapt the voltage and current limits of the battery. Moreover, the efficiency characteristic is compared to the one of a conventional battery with fixed cell topology and

Jan Engelhardt, Jan Martin Zepter, and Mattia Marinelli are with the Department of Wind and Energy Systems, Technical University of Denmark, Roskilde, Denmark (e-mail: janen@dtu.dk, jmwze@dtu.dk, matm@dtu.dk)

Luigi Piegari is with the Dipartimento di Elettronica, Informazione e Bioingegneria, Politecnico di Milano, Milan, Italy (e-mail: luigi.piegari@polimi.it)

Manuscript received —, 2023; revised —, 2023.

DC-DC converter. All in all, the study has the following key contributions:

- The paper presents the prototype of a battery string with reconfigurable topology on both string and cell level.
- A methodology for deriving the efficiency characteristic for the complete operating area of reconfigurable battery strings is proposed.
- The efficiency characteristic of the prototype is compared to the one of a conventional system with DC-DC converter, including a quantification of individual component losses.

The remainder of the paper is structured as follows. Section II describes the design and components of the prototype. Section III derives equations for calculating the efficiency of reconfigurable batteries, describes the benchmark system comprising a conventional system with DC-DC converter, and presents the case study. Section IV summarizes and discusses the numerical results, followed by concluding remarks in Section V.

II. Reconfigurable battery design

This section focuses on the developed prototype of a high-power reconfigurable battery. First, the system design is introduced, followed by the characterization of the different battery components.

A. System design

The battery described in the present study was developed in the framework of the research projects INSULAE and TOPChargE to explore the benefits of a reconfigurable battery in EV fast-charging applications. A battery module of this prototype is depicted in Fig. 1. The module contains 27 lithium-iron phosphate (LFP) cells with a nominal capacity of 100 Ah and a nominal voltage of 3.2 V [17]. The cell manufacturer Sinopoly specifies the maximum cell current for charging and discharging at 200 A and 300 A, respectively. The maximum cell voltage is reached at 3.65 V and the minimum cell voltage at 2.5 V. All cells within the module are connected in series via copper connectors and equipped with a controller responsible for monitoring the respective cell and actively controlling its connection state. The controller can either switch its cell in or out of the series connection, using two semiconductor switches. One switch comprises a parallel connection of four n-channel MOSFETs [18], with a drain-source voltage limit of $25\,\mathrm{V}$ and a drain current limit of $100\,\mathrm{A}$, respectively. The connection states of the two cell switches are inverse, meaning that one switch is active when engaging, and the other switch is active when bypassing the cell.

In order to match the voltage level of other DC components, such as EVs or PV systems, a battery string is formed by 12 modules. Fig. 2 shows the architecture of this string design. The battery string consists of two substrings with six series-connected modules each. The two substrings can be either connected in series or in parallel, to achieve different voltage and power capabilities. The substrings are connected in series by closing switch *SW1* and opening switches *SW2a* and *SW2b*. A parallel connection of the substrings is achieved by opening switch *SW1* and closing switches *SW2a* and *SW2b*. In either connection scheme, the string voltage can be adapted during operation by changing the number of engaged cells in each substring. This makes it possible to connect the battery string directly to other DC components, without the need for interfacing DC-DC converters. The power flow to or from the battery is controlled by changing the string voltage with respect to the voltage of the connected component (e.g. EV, PV). Furthermore, the state of charge (SOC) of the individual cells can be balanced by deciding which of the cells to engage and which to bypass, as demonstrated in [14]. Based on the total number of cells (324), the nominal cell voltage of $3.2\,\mathrm{V}$, and the nominal cell capacity of $100\,\mathrm{Ah}$, the estimated energy capacity of the battery string is $104\,\mathrm{kWh}$.

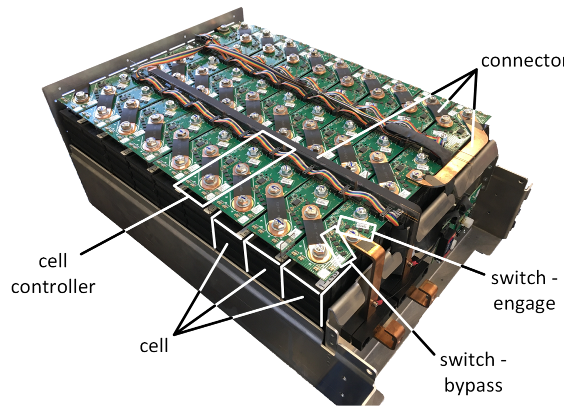

Fig. 1: Prototype of a reconfigurable battery module with 27 series-connected LFP cells. Each cell is equipped with a controller that can switch the cell in or out of the series connection.

B. System characterization

Fig. 3 shows the equivalent circuit of the string design, with series-connected modules and cells. The efficiency of the battery is mainly affected by ohmic resistances in the circuit that cause Joule losses when an electric current is applied. Switching losses of the MOSFETs are neglected in the present study, since cells are usually switched once every few minutes assuming a constant battery operating point. Hence,

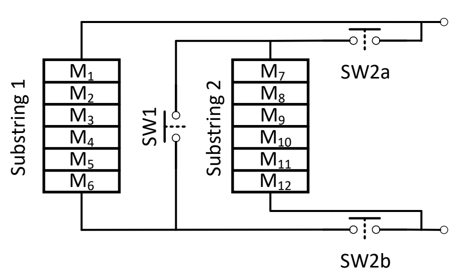

Fig. 2: String architecture comprising two substrings with six series-connected modules each. The substrings can be connected either in series or in parallel to adapt voltage and power capability.

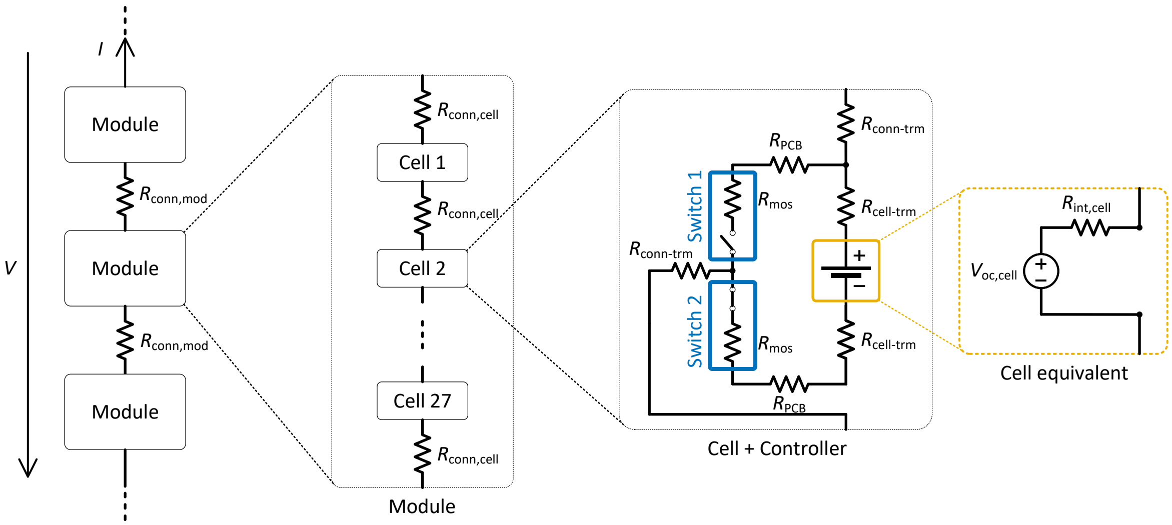

Fig. 3: Equivalent circuit of a reconfigurable battery string with series-connected modules and cells.

the equivalent circuit shown in Fig. 3 is the basis for the efficiency equations which will be derived in Section III-A. A representative cell was characterized to obtain the progressions of open-circuit voltage and internal resistance, as shown in Fig. 4. The open-circuit voltage was determined by measuring the voltage at currents of 3.5 A (discharging) and -3.5 A (charging), corresponding to C-rates of slightly above 1/30, and averaging the two curves. The cell capacity between minimum and maximum cell voltage was estimated at 106.9 Ah, thus approximately 7 % higher than stated in the datasheet. This value served as the base quantity for expressing the voltage as a function of the cell SOC with values between 0 % and 100 %. As indicated in Fig. 4, the cells are operated within 10 % (3.21 V) and 90 % (3.35 V) of their nominal capacity to stay within the linear region of the open-circuit voltage characteristic and to prevent over- or undercharging.

The dynamic behaviour of the cell was modelled with a second order Thevenin equivalent circuit. Pulse charge experiments were conducted to estimate the values of the RC branches at different SOC values within the operating area, for both charging and discharging. The current was controlled with a DC power supply [19], with pulses of 100 A (-100 A for charging) for 6 minutes followed by a relaxation time of 90 minutes. The voltage was measured with a NI-9215 module [20]. For the present study, the efficiency is calculated considering static operating points. The internal cell resistance $R_{\text{int,cell}}$ is considered as the sum of R_0 and R_1. As elaborated in [21], resistance R_2 is neglected for the power loss estimation, since the time constant R_2C_2 has an average value of 230 minutes. In comparison, the time constant R_1C_1 has an average value of 1.6 minutes.

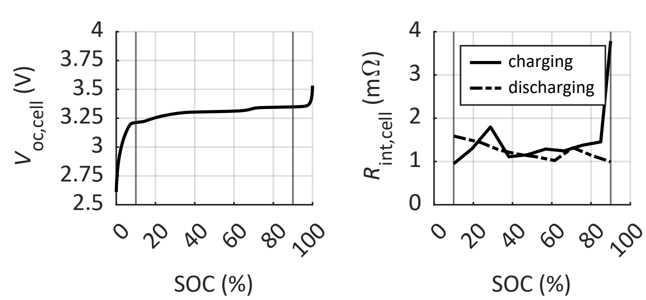

Fig. 4: Open-circuit voltage and internal resistance $(R_0 + R_1)$ of one LFP cell as a function of the SOC.

Besides Joule losses inside the cells, additional losses are caused by the elements used to integrate the cells in the battery system. As seen in Fig. 1, the cells are linked via copper connectors that are bolted on the printed circuit board (PCB) terminals of the cell controller. This bolting resistance $R_{\text{conn-trm}}$ is always present, independent of the cell activation state. If a cell is bypassed, Joule losses are caused by the conducting path of the PCB, R_{PCB}, and the on-state resistance of Switch 1, R_{mos} (see Fig. 3). In contrast, if a cell is active, the current flows through the internal cell resistance $R_{\text{int,cell}}$, the bolting resistances between cell and PCB terminals, $R_{\text{cell-trm}}$, the resistance of the PCB, R_{PCB}, and the on-state resistance of Switch 2, R_{mos}. The resistances of PCB and connecting terminals (at a torque of 12 N m) were measured via the 4-point probe method at the obtained values listed in Table I. The measurements were performed using a BK-Precision 8601 as current source [22], with an accuracy of $\pm 0.35\,\%$ for the applied current of 10 A. The voltage was measured using a Fluke 8846A [23], with an accuracy of $\pm\,(0.0035\,\% + 0.5\,\mu\text{V})$ for the given measurement range. The switch resistance R_{mos} derives from the parallel connection of four MOSFETs in on-state. The copper connectors used to link cells and modules have a cross-sectional area of $66\,\text{mm}^2$ and a specific resistivity of $0.0168\,\Omega \cdot \text{mm}^2/\text{m}$. The connectors have different lengths and, consequently, different resistances, as listed in Table I.

In case of parallel operation of the two substrings, the voltages of both substrings must be matched before connecting. The resulting inrush current is determined by the voltage difference between the two substrings and the total resistance in the circuit. Typically, the maximum voltage difference is equal to $V_{\text{oc,cell}}/2$, while the resistance is given by the equivalent circuit shown in Fig. 3. Assuming both substrings have

TABLE I: Ohmic resistances of battery components.

Symbol	Value	Description
$R_{\text{cell-trm}}$	$30\,\mu\Omega$	Terminal resistance cell-PCB
$R_{\text{conn-trm}}$	$27\,\mu\Omega$	Terminal resistance connector-PCB
R_{PCB}	$120\,\mu\Omega$	PCB resistance
R_{mos}	$145\,\mu\Omega$	On-state resistance of switch
$R_{\text{conn,cell}}$	$24 \times 17\,\mu\Omega$ $1 \times 59\,\mu\Omega$ $1 \times 62\,\mu\Omega$ $1 \times 97\,\mu\Omega$ $1 \times 194\,\mu\Omega$	Resistances of cell connectors, with different values due to different connector lengths. Numbers of cell connectors are given per module
$R_{\text{conn,mod}}$	$10 \times 71\,\mu\Omega$ $3 \times 571\,\mu\Omega$	Resistances of module connectors

an average SOC of $50\,\%$ and a target voltage of $350\,\text{V}$, the resulting inrush current is estimated at $6.76\,\text{A}$, corresponding to a C-rate of 0.0676. While such current levels are easy to handle, the presented design could also be complemented with inrush current limiters [24], [25], to further mitigate the impact when switching from series to parallel configuration.

III. Characterization of Battery Efficiency

The methodology is structured as follows. First, general equations for the efficiency are derived taking into account the reconfigurable design. Second, a benchmark system is introduced which allows to compare the efficiency characteristic of the reconfigurable battery to that of a conventional solution. Finally, the case study is described.

A. Efficiency of reconfigurable battery

The efficiency of a reconfigurable battery with series-connected cell topology is directly influenced by the number of active cells. In particular, the two possible activation states of each cell must be considered. The resistance of each cell, including its controller, can be represented with a constant plus a variable part. Since always one of the two switches per cell is in on-state mode, and the PCB resistance is the same for either cell connection state, the total cell resistance (cell + controller) has a constant part of

$$R_{\text{cell,const}} = 2 \cdot R_{\text{conn-trm}} + R_{\text{PCB}} + R_{\text{mos}}. \tag{1}$$

In case a cell is enabled, a variable part is added to the total resistance:

$$R_{\text{cell,var}} = 2 \cdot R_{\text{cell-trm}} + R_{\text{int,cell}}, \tag{2}$$

where $R_{\text{int,cell}}$ is the SOC dependent internal cell resistance. The connector resistances of cells and modules, together with the constant part of the cell resistances, can be summarized as a constant part of the battery resistance:

$$R_{\text{conn,batt}} = \sum R_{\text{conn,mod}} + \sum R_{\text{conn,cell}} \tag{3}$$

$$R_{\text{batt,const}} = N_{\text{cells}} \cdot R_{\text{cell,const}} + R_{\text{conn,batt}} \tag{4}$$

The battery voltage depends on the current and the number of active cells, and is formulated as

$$V_{\text{batt}} = \sum_{i=1}^{N_{\text{cells}}} \left(V_{\text{oc,cell},i} - R_{\text{cell,var},i} \cdot I_{\text{batt}}\right) \cdot \Gamma_{\text{cell},i} - R_{\text{batt,const}} \cdot I_{\text{batt}}, \tag{5}$$

where $\Gamma_{\text{cell},i}$ is the connection state ("1" engaged, "0" bypassed) of the i-th cell. The current I_{batt} is defined in generator convention, with positive values corresponding to discharging, and negative values to charging. Under the assumption that all cells show the same characteristic and that the BMS balances their SOC during operation, the equation can be simplified to

$$V_{\text{batt}} = N_{\text{act}} \cdot \left(V_{\text{oc,cell}} - R_{\text{cell,var}} \cdot I_{\text{batt}}\right) - R_{\text{batt,const}} \cdot I_{\text{batt}}, \tag{6}$$

where N_{act} is the number of active cells. The battery power is defined as $P_{\text{batt}} = V_{\text{batt}} \cdot I_{\text{batt}}$, while the Joule losses are given as

$$P_{\text{loss}} = I_{\text{batt}}^2 \cdot \left(N_{\text{act}} \cdot R_{\text{cell,var}} + R_{\text{batt,const}}\right). \tag{7}$$

Finally, based on Joule losses and total battery power, the battery efficiency is formulated as

$$\eta = \begin{cases} \frac{P_{\text{batt}} + P_{\text{loss}}}{P_{\text{batt}}}, & \text{for } P_{\text{batt}} < 0 \\ 1, & \text{for } P_{\text{batt}} = 0 \\ \frac{P_{\text{batt}}}{P_{\text{batt}} + P_{\text{loss}}}, & \text{for } P_{\text{batt}} > 0. \end{cases} \tag{8}$$

For the present string architecture with two substrings, which can be connected either in series or in parallel, the two cases must be considered independently. In case of the series connection, the equations presented above are directly applicable. In case of the parallel connection, the power losses are first calculated for a single substring, assuming the full battery voltage, V_{batt}, but only half the battery current, $I_{\text{batt}}/2$. Subsequently, the battery efficiency is calculated considering twice the power losses, $2 \cdot P_{\text{loss}}$.

B. Benchmark system description

Conventional batteries with fixed cell topology do not have the intrinsic capability of adapting their voltage during operation. Thus, they require power converters for connecting to other components or systems. Fig. 5 compares the two distinct system designs.

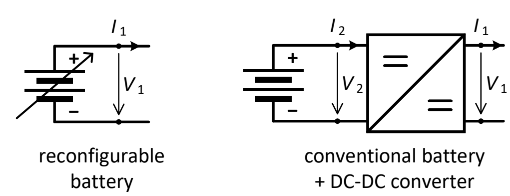

Fig. 5: Comparison between reconfigurable battery and conventional system. The latter comprises a fixed-topology battery with DC-DC converter.

In the present study, the conventional system serves as a benchmark to evaluate the efficiency characteristics of the reconfigurable battery design. The comparison is conducted for the use case of battery-powered EV fast charging, as this is the primary intended application of the developed prototype. Hence, the voltage V_1 must match the considered use case, i.e., power transfer from the stationary battery to an EV. Currently, the majority of current EV models relies on 400 V charging systems. Based on the minimum and maximum cell voltage [17], the two substrings of the reconfigurable battery will be operated in parallel, since this

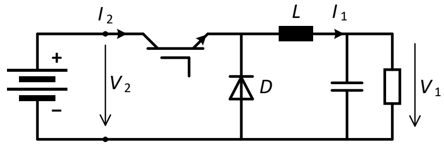

Fig. 6: Buck converter circuit of the benchmark system.

will achieve voltages between $405\,\text{V}$ and $591.3\,\text{V}$ in case all cells are engaged.

For the benchmark system, assumptions for both battery and DC-DC converter must be made. The conventional battery is considered with the same cell configuration as the reconfigurable battery, thus, with a 162s2p topology (two branches of 162 series-connected cells—6 modules with 27 cells each). However, it does not require the elements necessary for engaging and bypassing of cells. Compared to the equivalent circuit shown in Fig. 3, the resistances for the MOSFETS, R_{mos}, for the PCBs, R_{PCB}, and for the interface of connectors and PCBs, $R_{\text{conn-trm}}$, are therefore not considered. The components of the DC-DC converter are selected based on the voltage and current limits. The voltage on the battery side, V_2, can range between $405\,\text{V}$ and $591.3\,\text{V}$ at currents of up to $600\,\text{A}$. To achieve a suitable voltage range for EVs, the output voltage of the DC-DC converter, V_1, is defined to range between $250\,\text{V}$ and $420\,\text{V}$. Fig. 6 shows the layout of the considered buck converter, while Table II details the parameters of the individual components. The calculation of power losses follows the methodology presented in [26], assuming a switching frequency of $f_s = 10\,\text{kHz}$.

TABLE II: Buck converter parameters.

Component	Symbol	Value	Description
Inductor [27] (267p40p)	R_i	$14.69\,\text{m}\Omega$	Internal resistance
	L_i	$100.13\,\mu\text{H}$	Inductance
IGBT module [28] (2 in parallel)	R_{ds}	$0.8\,\text{m}\Omega$	Drain to source typical resistance
	R_d	$1.45\,\text{m}\Omega$	Internal diode resistance
	V_{ce0}	$0.4\,\text{V}$	Collector-emitter saturation voltage
	V_{cc}	$300\,\text{V}$	Collector-emitter test voltage
	I_{cc}	$300\,\text{A}$	Collector test current
	E_{on}	$12.8\,\text{mJ}$	Turn on switching energy per pulse
	E_{off}	$29.8\,\text{mJ}$	Turn off switching energy per pulse
	Q_{rr}	$21\,\mu\text{C}$	Reverse recovery charge

The auxiliary consumption of the two system designs is considered similar and, therefore, neglected in the present analysis. Auxiliary consumption is mainly determined by the equipment used for monitoring the battery (microcontrollers, sensors, drivers) and the thermal management system [29]. Hence, it largely depends on external factors such as the usage pattern or ambient conditions. In all Lithium-based batteries, the battery management system must continuously monitor all cells [30], independent of whether the design has a fixed or variable cell topology.

C. Case study

A sensitivity analysis is conducted to determine the impact of different battery setpoints on the efficiency. The analysis is designed to cover the complete operating area of the reconfigurable battery. The investigation is made for both the series and parallel connection of the two substrings. The number of active cells is varied between $N_{\text{act}} = 1...324 \in \mathbb{N}$, and the current I_{batt} is varied in 0.1 A steps between the operating cell current limits for charging (-200 A) and discharging (300 A). Furthermore, the analysis is performed for different SOC values, which changes the cell characteristic according to Fig. 4. Based on equations (1) – (8), the other state variables (voltage, power, etc.) are derived using the physical properties of the real system. Besides efficiency considerations, operating limits imposed by the maximum cell number, as well as cell current and voltage limits are investigated. Furthermore, the same analysis is performed with the benchmark system, considering a battery with fixed topology and DC-DC converter.

IV. Results and Discussion

This section presents and discusses the results and is divided into three parts. First, the progressions of battery efficiency and number of active cells are derived for different voltage levels and as a function of the power setpoint. Second, efficiency maps for the complete operating area are presented, showing the impact of power, voltage, and SOC on the efficiency. Third, the efficiency characteristic is compared to the benchmark system, including a breakdown of component losses for different operating setpoints.

A. Efficiency at discrete voltage levels

Fig. 7 shows the efficiency of the battery system in dependency of the power, together with the number of active cells needed to achieve the respective setpoints. The results were obtained at a battery SOC of 50 %, and the substrings are connected in series. Efficiencies and cell numbers are given for discrete voltage levels between 300 V and 1000 V, which is the range in which the prototype is usually operated. In the graphs, the operating limits of charging and discharging current, as well as the maximum number of cells are indicated. The results show that higher voltage levels lead to higher efficiencies. This is because for the same power setpoint, the current is lower at higher voltage levels, leading to lower Joule losses. The graph further shows that higher power levels can be achieved during discharging, since the maximum discharging current of the cells, $I_{\text{dis,max}}$, is higher than the maximum charging current, $I_{\text{ch,max}}$. The two lines for the current limits mark operational boundaries of the battery string, as highlighted in the plot.

The lower subplot shows the number of cells that need to be engaged to achieve the respective voltage levels, as a function of the power setpoint. The required number of active cells is lower for charging and increases continuously with the power. At high voltage and power levels (top right corner), the number of active cells reaches the maximum cell number N_{cells} in the battery string. No additional cells can be engaged from this point, marking another operational limit of the system.

B. Efficiency maps

In the previous subsections, the general characteristic of the reconfigurable battery string was shown and discussed for

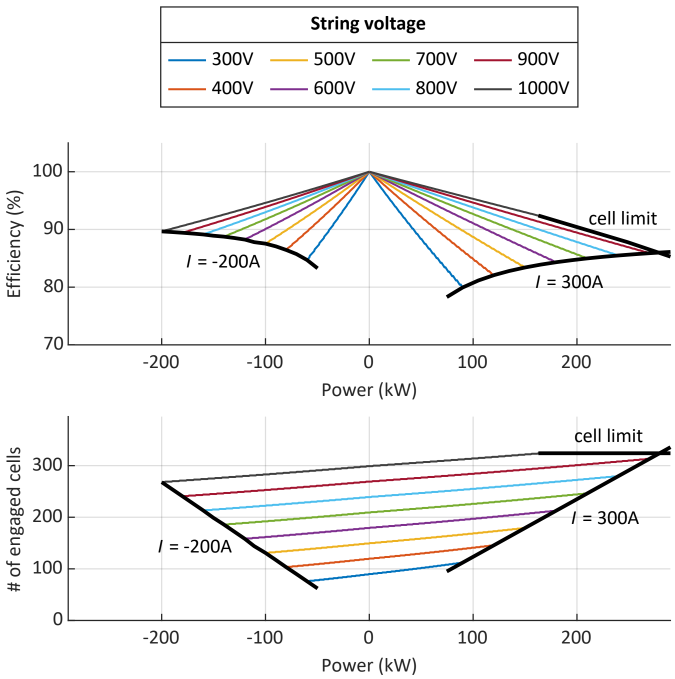

Fig. 7: Battery efficiency and number of engaged cells at discrete voltage levels, as a function of the power setpoint.

discrete voltage levels in steps of 100 V. The following analysis utilizes the fine resolution of the performed sensitivity analysis to develop continuous efficiency maps. Fig. 8 presents the obtained values as a contour map with dependency on battery power and voltage for different SOC levels, namely at 20 %, 50 %, and 80 %.

The outline of the contour map is enclosing the operating area of the battery string. The maximum charging current is restricting the area from the left-hand side, while the maximum discharging current is the restricting factor on the right-hand side. The maximum number of available cells is eventually imposing a limit to the overall string voltage, thus the upper edge of the area. Generally, the efficiency is highest for low absolute values of the power. For a given battery power, higher voltage levels achieve higher efficiencies as already discussed in Section IV-A.

Furthermore, the contour maps for the different SOC values reveal differences, mainly due to the dependency of the cell resistance on the charge level. Since the cell resistance is increasing during discharge when approaching the lower SOC limit, the efficiency map in Fig. 7 (a) reveals a steeper decline with increasing discharge power. Besides the higher density of contour lines, this effect is particularly apparent at the right edge, where the efficiency values are considerably lower compared to the other two subplots. Similarly, during charging, the cell resistance experiences an increase when approaching the upper SOC limit, visible in Fig. 7 (c). Furthermore, the cell resistance has a direct impact on the outline of the operating area, in particular on the upper edge. For higher values of the cell resistance, the upper limit, indicating the voltage achieved by engaging all cells, drops more sharply. This behaviour is caused by the fact that during discharging the voltage drop along all resistive elements must be provided by the engaged cells. With higher cell resistances, more cells need to be active to achieve the required voltage at the battery terminals. Hence, the maximum number of cells is reached earlier compared to discharging with lower cell resistances. Conversely, during charging the voltage drop along the resistive elements adds to the open-circuit voltages of all engaged cells. As a result, a lower number of active cells is needed to achieve the required battery voltage level. Consequently, in the case of charging, higher cell resistances allow the battery to achieve higher voltage levels but also lead to lower efficiencies. It is noteworthy that when approaching the upper and lower charge limits of the cells, additional operating limits will be imposed by the maximum and minimum cell voltage. In this case, the charging or discharging current has to be restricted so that the cell voltage limits are not violated.

C. Comparison to conventional system

The modular string architecture with two substrings enables a transformation of the operating area by connecting the two substrings in parallel. In this operating mode, the string current is shared by the two substrings. While the parallel connection decreases the string voltage, it increases the power capability at low voltage levels. This change in the operating area is apparent from the efficiency map in Fig. 9 (a). The efficiency characteristic of the benchmark system introduced in Section III-B is shown in Fig. 9 (b). The two battery designs reveal clear differences in the operating area. While the benchmark system is restricted to voltage values between 250 V and 420 V, the reconfigurable battery has a significantly wider voltage range, reaching from 0 V up to 587 V.

Furthermore, the progression of the efficiency is different for the two systems. While the reconfigurable battery shows a decreasing efficiency with increasing absolute power, the efficiency characteristic of the benchmark system is influenced by the DC-DC converter leading to a sharp decline when approaching zero power. To quantify the difference between the two systems, Fig. 10 shows the absolute difference in efficiency, in percentage points, with focus on the more narrow voltage range of the benchmark system. The contour map reveals higher efficiencies of the reconfigurable battery at low power values, while the benchmark system performs better at high power values. The turning point where both systems have the same efficiency is dependent on the voltage setpoint. During charging, the turning point ranges from 31 kW at 250 V to 57 kW at 420 V, with an average value of 44.6 kW. During discharging, the turning point ranges from 31 kW at 250 V to 61 kW at 420 V, with an average value of 46.7 kW.

The models of both systems further allow to allocate the power losses to the different system components, as presented in Fig. 11. The comparison is done for two different setpoints, the first at 350 V/25 kW, and the second at 350 V/100 kW. All in all, the total power losses are significantly higher at the second operating setpoint. While the reconfigurable battery has lower power losses at 25 kW, the conventional battery design performs better at 100 kW, as discussed previously. The losses of the reconfigurable battery are divided into losses caused

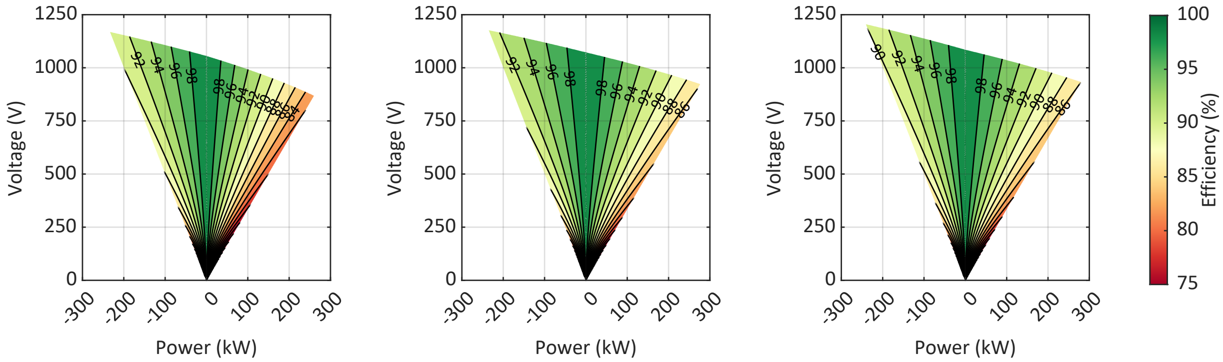

(a) SOC = 20 %
(b) SOC = 50 %
(c) SOC = 80 %

Fig. 8: Contour maps for the battery efficiency as a function of power and voltage for different SOC levels. The operating area is restricted by the maximum charging current (left edge), the maximum discharging current (right edge), and the maximum number of active cells (upper edge).

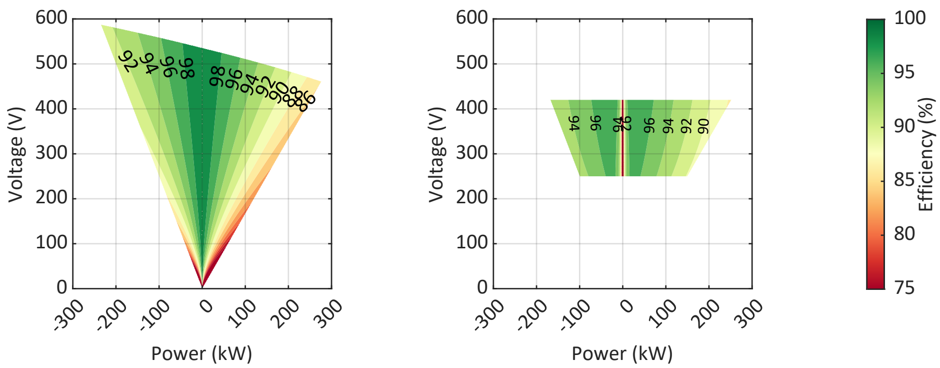

(a) reconfigurable battery
(b) benchmark system

Fig. 9: Efficiency contour maps for parallel connection of the substrings at an SOC of 50 %. The subfigures show efficiency and operating area for (a) reconfigurable battery, and (b) conventional battery + DC-DC converter.

by (i) battery cells including cell terminals, (ii) connectors, (iii) MOSFETs, and (iv) PCBs, including connector terminals. While the benchmark system does not have MOSFET or PCB losses due to its fixed cell topology, the DC-DC converter causes (v) switching and (vi) conductive losses.

Particularly at 25 kW, switching losses are the dominant source of losses for the benchmark system. In contrast, at 100 kW, the cells contribute to 61.5 % of the power losses of the benchmark system, while conduction and switching losses contribute to 22.4 % and 14.1 %, respectively. Connector losses only add a minor contribution of 2 %. In case of the reconfigurable battery, the cells cause 70 % of the overall losses at 100 kW, PCBs 14.6 %, MOSFETs 12.2 %, and connectors 3.2 %. Although the losses of the components enabling the reconfigurable cell topology (PCBs, MOSFETs) level out the converter losses at this operating setpoint, the reconfigurable battery has higher cell and connector losses than the benchmark system. While the engaged cells in the reconfigurable battery always experience the full current I_1, the cells of the conventional battery experience the lower current I_2 due to the conversion ratio of the buck converter. In this regard, the benchmark system benefits from being designed for a specific voltage range, while the operating area of the reconfigurable battery is significantly broader. Hence, a future study could compare the presented string design to a conventional battery system with the same operating area.

D. Further considerations

Besides efficiency considerations, other relevant aspects are the power and energy density of the two designs. The module shown in Fig. 1 has a volume of 76.90 L. The total string volume comprising the grouping of 12 modules, management system (57.24 L), and cross-over module (38.31 L) for series/parallel configuration, is 1018.35 L. Considering the maximum discharge power of 280 kW and the energy capacity of 104 kWh, the volumetric power and energy densities of the prototype system are 274.95 W/L and 102.12 Wh/L, respectively. The conventional battery modules are considered with the same volume, since the switches of the reconfigurable modules are integrated in the cell monitoring equipment present in all Li-ion battery systems, thus, adding no extra volume. Similarly, also conventional battery systems require a management system with the same key functionalities (e.g., safety, monitoring, cell balancing). While the conventional system does not include any cross-over module, DC-DC converters with the specifications defined in Section III-B have a similar volume [31], [32]. Hence, the corresponding volumetric power and energy densities of the conventional design are $245.5\,\mathrm{W/L}$ and $102.12\,\mathrm{Wh/L}$, respectively, which is comparable to those of commercial LFP-based battery systems [33].

Further considerations center around the application of batteries in integrated systems, including the compatibility and coordination with other units. In this regard, the broad voltage range of the reconfigurable string allows the connection to various DC components with diverse operating voltages, such as $400\,\mathrm{V}$ and $800\,\mathrm{V}$ EVs, PV systems, or AC grid-connected inverters. This facilitates novel microgrid architectures that do not require any DC-DC converters [34]. Another candidate application are traction batteries for EVs, where a broad power range is required. In this use case, the average power consumption is considerably lower than the rated power [35], [36], hence, the higher efficiency of the reconfigurable design at low power values is advantageous. To this end, a future study could compare reconfigurable and conventional batteries in different applications, considering additional aspects such as costs, reliability, and control complexity.

V. Conclusion

The present paper characterizes a prototype of a reconfigurable battery for high-power applications. Each of the 324 cells is equipped with a cell controller that can switch the cell in or out of the series connection. Consequently, the battery has the intrinsic capability to adapt its voltage during operation and can be directly connected to other DC components like EVs or PV systems, without the need of interfacing power converters. General equations for calculating the battery efficiency were derived and served as the basis for developing efficiency maps for the complete operating area of the prototype. The battery can adapt its voltage between $0\,\mathrm{V}$ and up to $1200\,\mathrm{V}$, and reaches power values of $240\,\mathrm{kW}$ for charging, and $280\,\mathrm{kW}$ for discharging. A sensitivity analysis was performed to determine the influence of battery voltage, power, and SOC on the efficiency. The results show that for a given power setpoint, higher voltage levels allow to achieve better efficiencies, while the highest efficiencies are achieved at low power values. A comparison to a conventional battery with DC-DC converter showed that reconfigurable battery can operate at a wider voltage range and achieves a better efficiency up to an average power of $44.6\,\mathrm{kW}$ during charging, and $46.7\,\mathrm{kW}$ during discharging. Conversely, the conventional system performs better above these thresholds. All in all, the introduced method of estimating the efficiency characteristic can be applied to other battery specifications, for instance, different cell numbers or cell chemistries. This makes the model a suitable tool for designing and sizing reconfigurable batteries for specific applications. Furthermore, the results and insights presented in this paper can serve as an input for models that take a more high-level view on the system. In particular, the efficiency maps can be used to develop and test energy management strategies of reconfigurable batteries in various applications, as they capture operating area and efficiency as a function of power, voltage, and SOC.

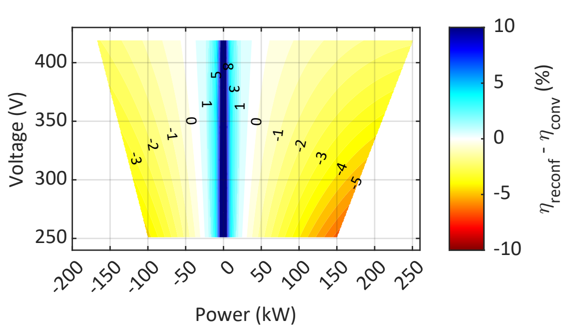

Fig. 10: Absolute efficiency difference between reconfigurable battery and benchmark system.

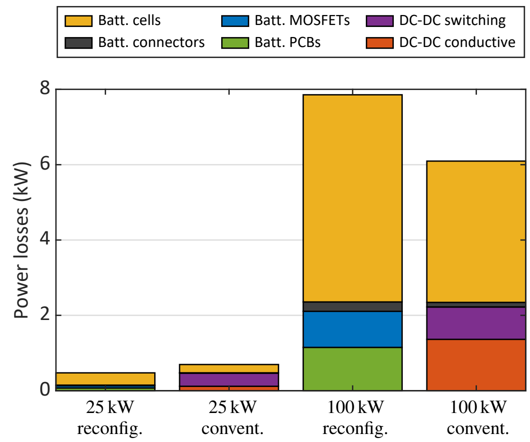

Fig. 11: Comparison of component power losses at discrete operating points for both the reconfigurable and the conventional battery system.

Acknowledgements

This work has received funding from the H2020 INSULAE project under the Grant Agreement No. 824433, and from the IFD funded TOPChargE project under the Grant Agreement No. 9090-00035A.

References

[1] M. Ahmadi, O. B. Adewuyi, M. S. Danish, P. Mandal, A. Yona, T. Senjyu, "Optimum coordination of centralized and distributed renewable power generation incorporating battery storage system into the electric distribution network," *Int. J. Electr. Power Energy Syst.*, vol. 125, 2021. https://doi.org/10.1016/j .ijepes.2020.106458.

[2] S. Grillo, M. Marinelli, S. Massucco, F. Silvestro, "Optimal Management Strategy of a Battery-Based Storage System to Improve Renewable Energy Integration in Distribution Networks," *IEEE Trans. Smart Grid*, vol. 3, no. 2, pp. 950-958, June 2012. doi: 10.1109/TSG.2012.2189984 .

[3] D. D. Simone, L. Piegari, "Integration of stationary batteries for fast charge EV charging stations," *Energies*, vol. 12, no. 24, 2019. https://doi.org/10.3390/en12244638

[4] M. M. Mahfouz, M. R. Iravani, "Grid-Integration of Battery-Enabled DC Fast Charging Station for Electric Vehicles," *IEEE Trans. Energy Convers.*, vol. 35, no. 1, pp. 375–385, March 2020. doi: 10.1109/TEC.2019.2945293 .

[5] G. Liu, Y. Xue, M. S. Chinthavali, K. Tomsovic, "Optimal Sizing of PV and Energy Storage in an Electric Vehicle Extreme Fast Charging Station," in *2020 IEEE Power & Energy Society Innovative Smart Grid Technologies Conference (ISGT)*, pp. 1-5. doi: 10.1109/ISGT45199.2020.9087792 .

[6] J.A. Domínguez-Navarro, R. Dufo-López, J.M. Yusta-Loyo, J.S. Artal-Sevil, J.L. Bernal-Agustín, "Design of an electric vehicle fast-charging station with integration of renewable energy and storage systems," *Int. J. Electr. Power Energy Syst.*, vol. 105, pp. 46-58, 2019. https://doi.org/10.1016/j.ijepes.2018.08.001 .

[7] M. R. Khalid, M. S. Alam, A. Sarwar, M.S. Jamil Asghar, "A Comprehensive review on electric vehicles charging infrastructures and their impacts on power-quality of the utility grid," *eTransportation*, vol. 1, 2019. https://doi.org/10.1016/j.etran.2019.100006 .

[8] D. Sbordone, I. Bertini, B. D. Pietra, M. C. Falvo, A. Genovese, L. Martirano, "EV fast charging stations and energy storage technologies: A real implementation in the smart micro grid paradigm," *Electr. Power Syst. Res.*, vol. 120, pp. 96–108, 2015. https://doi.org/10.1016/j.epsr.2014.07.033 .

[9] Z. Wei, J. Zhao, H. He, G. Ding, H. Cui, and L. Liu, "Future smart battery and management: Advanced sensing from external to embedded multi-dimensional measurement," *Journal of Power Sources*, vol. 489, p. 229462, Mar. 2021. doi: 10.1016/j.jpowsour.2021.229462 .

[10] S. Ci, N. Lin, and D. Wu, "Reconfigurable Battery Techniques and Systems: A Survey," *IEEE Access*, vol. 4, pp. 1175–1189, 2016. doi: 10.1109/access.2016.2545338 .

[11] S. Muhammad, M. U. Rafique, S. Li, Z. Shao, Q. Wang, and X. Liu, "Reconfigurable Battery Systems," ACM Transactions on Design Automation of Electronic Systems, vol. 24, no. 2, pp. 1–27, 2019. doi: 10.1145/3301301 .

[12] F. Ji, L. Liao, T. Wu, C. Chang, and M. Wang, "Self-reconfiguration batteries with stable voltage during the full cycle without the DC-DC converter," *Journal of Energy Storage*, vol. 28, p. 101213, Apr. 2020. doi: 10.1016/j.est.2020.101213 .

[13] J. Engelhardt, J. M. Zepter, T. Gabderakhmanova, and M. Marinelli, "Energy management of a multi-battery system for renewable-based high power EV charging," *eTransportation*, vol. 14, p. 100198, Nov. 2022. doi: 10.1016/j.etran.2022.100198 .

[14] J. Engelhardt, J. M. Zepter, T. Gabderakhmanova, G. Rohde, M. Marinelli, "Double-String Battery System with Reconfigurable Cell Topology Operated as a Fast Charging Station for Electric Vehicles," *Energies*, vol. 14, no. 9, 2021. https://doi.org/10.3390/en14092414 .

[15] A. Bowen, J. Engelhardt, T. Gabderakhmanova, M. Marinelli, and G. Rohde, "Battery Buffered EV Fast Chargers on Bornholm: Charging Patterns and Grid Integration," *2022 57th International Universities Power Engineering Conference*, IEEE, Aug. 30, 2022. doi: 10.1109/upec55022.2022.9917690 .

[16] J. Engelhardt, J. M. Zepter, T. Gabderakhmanova, and M. Marinelli, "Efficiency Characteristic of a High-Power Reconfigurable Battery with Series-Connected Topology," *2022 International Power Electronics Conference*, IEEE, May 15, 2022. doi: 10.23919/ipec-himeji2022-ecce53331.2022.9807176.

[17] Sinopoly Battery, "Model: SP-LFP100AHA," datasheet. [Online]. Available: http://www.sinopolybattery.com/userfiles/files/SP-LFP100AHA.pdf. [Accessed: Oct. 25, 2021].

[18] Vishay Intertechnology Inc., "SIRA20DP Product information," [Online]. Available: https://www.vishay.com/docs/76212/sira20dp.pdf. [Accessed: Oct. 17, 2023].

[19] Elektro-Automatik, "Operating Guide PSI 9000 Power Supply Series," model EA-PSB 10200-420 4U 30000W. [Online]. Available: https://elektroautomatik.com/shop/media/pdf/d7/5f/9d/30000800_EN.pdf. [Accessed: Mar. 4, 2022].

[20] National Instruments, "NI 9215 Datasheet," 2016. [Online]. Available: https://www.ni.com/pdf/manuals/373779a_02.pdf. [Accessed: Mar. 4, 2022].

[21] J. Engelhardt, "Reconfigurable Batteries in Electric Vehicle Fast Chargers: Towards Renewable-Powered Mobility," PhD thesis, Technical University of Denmark, 2022. doi: 10.11581/dtu.00000254 .

[22] B&K Precision Corporation, "Programmable DC Electronic Loads - Model 8601," [Online]. Available: https://www.bkprecision.com/products/dc-electronic-loads/8601-250-w-programmable-dc-electronic-load.html. [Accessed: Oct. 24, 2021].

[23] Fluke Corporation, "Fluke 8845A 6.5 Digit Precision Multimeter," [Online]. Available: https://www.fluke.com/en-us/product/precision-measurement/bench-instruments/fluke-8845a-8846a. [Accessed: Oct. 24, 2021].

[24] E.-J. Lee, J.-H. Ahn, S.-M. Shin and B.-K. Lee, "Comparative analysis of active inrush current limiter for high-voltage DC power supply system," In: *2012 IEEE Vehicle Power and Propulsion Conference*, Seoul, 2012, pp. 1256-1260, doi: 10.1109/VPPC.2012.6422710.

[25] N. Tashakor, B. Arabsalmanabadi, T. Ghanbari, E. Farjah, and S. Götz, "Start-up circuit for an electric vehicle fast charger using SSICL technique and a slow estimator," in: *IET Gener. Transm. Distrib.*, vol. 14, pp. 2247-2255, 2020. doi: 10.1049/iet-gtd.2019.1477

[26] C. Wang, R. Xiong, H. He, X. Ding, and W. Shen, "Efficiency analysis of a bidirectional DC/DC converter in a hybrid energy storage system for plug-in hybrid electric vehicles," *Applied Energy*, vol. 183, pp. 612–622, Dec. 2016. doi: 10.1016/j.apenergy.2016.08.178 .

[27] TDK Corporation, "ERU chokes - ERU 25, helically wound," datasheet. [Online]. Available: https://product.tdk.com/system/files/dam/doc/product/inductor/inductor/smd/data_sheet/30/db/ind_2008/b82559_a025.pdf. [Accessed: May 18, 2023].

[28] Mitsubishi Electric Corporation, "CM300DY-13T," datasheet. [Online]. Available: https://www.mitsubishielectric.com/ semiconductors/content/product/powermodule/igbt/t_series/cm300dy-13t_e.pdf. [Accessed: May 18, 2023].

[29] M. Schimpe, M. Naumann, N. Truong, H.C. Hesse, S. Santhanagopalan, A. Saxon, and A. Jossen, "Energy efficiency evaluation of a stationary lithium-ion battery container storage system via electro-thermal modeling and detailed component analysis," In: *Applied Energy*, vol. 210, pp. 211-229, 2018. doi: 10.1016/j.apenergy.2017.10.129 .

[30] R. Xiong, L. Li, and J. Tian, "Towards a smarter battery management system: A critical review on battery state of health monitoring methods," In: *Journal of Power Sources*, vol. 405, pp. 18–29, 2018. doi: 10.1016/j.jpowsour.2018.10.019 .

[31] ZEKALABS Ltd., "RedPrime 200kW, 850V DC-DC Converter," [Online]. Available: https://zekalabs.com/products/non-isolated-high-power-converters/dc-dc-converter-200kw-850v/. [Accessed: Oct 18, 2023].

[32] ApECOR, "EV Bi-Directional DC-DC," datasheet [Online]. Available: http://apecor.com/pages/products/highpower/apecor_ev_bidirectional_dcdc.pdf [Accessed: Oct 18, 2023].

[33] CATL, "CATL Energy Storage System Solutions and Product Brochure," [Online]. Available: https://www.catl.com/en/ess/ [Accessed: Oct 18, 2023].

[34] J. Engelhardt, S. Grillo, L. Calearo, M. Agostini, M. Coppo, and M. Marinelli, "Optimal control of a DC microgrid with busbar matrix for high power EV charging," In: *Electric Power Systems Research*, vol. 224, p. 109680, 2023. doi: 10.1016/j.epsr.2023.109680 .

[35] A. Thingvad and M. Marinelli, "Influence of V2G Frequency Services and Driving on Electric Vehicles Battery Degradation in the Nordic Countries," In: *Proceedings of EVS 31 & EVTeC 2018*, Kobe, Japan, 2018.

[36] C. Fiori, K. Ahn, and H.A. Rakha, "Power-based electric vehicle energy consumption model: Model development and validation," In: *Applied Energy*, vol. 168, pp. 257-268, 2016. doi: 10.1016/j.apenergy.2016.01.097 .